Hierarchical Nitrogen-doped Mo$_2$C Nanoparticle-in-microflower Electrocatalyst: in Situ Synthesis and Efficient Hydrogen-evolving Performance in Alkaline and Acidic Media

Yongli Sun[+],[a] Feifei Peng[+],[a] Luhong Zhang,[a] Bin Jiang,[a] Haozhen Dou,[a] Na Zhang,[a] Mi Xu,[a] and Na Yang*[a]

Herein, a novel 6~9 nm nitrogen-doped Mo$_2$C nanoparticles (Mo$_2$C P) homogeneously decorated on 3D porous nitrogen-doped Mo$_2$C microflowers (Mo$_2$C F) were prepared in situ to form 0D/3D Mo$_2$C P/Mo$_2$C F. This special structure combines the advantages of Mo$_2$C P and porous Mo$_2$C F to provide a high density of reaction sites and facilitate the diffusion of electrolyte and hydrogen. Mo$_2$C P/Mo$_2$C F exhibits excellent HER performance in both alkaline and acidic solutions. It only requires an overpotential of 96 and 118 mV to achieve a current density of 10 mA cm^{-2} (η_{10}) in 1.0 M KOH and 0.5 M H$_2$SO$_4$, respectively. Moreover, it works better than commercial Pt/C at high current densities in 1.0 M KOH. The Tafel slopes are less than 50 mV/dec in both media, suggesting an obviously fast HER kinetics. Additionally, this study presents a universally applicable method to prepare M$_x$C P/Mo$_2$C F (M≡Fe, Co, V) for different applications.

1. Introduction

The superiority of cleaning and sustainable regeneration as well as high energy density has prompted hydrogen to become one of the most promising alternatives to traditional fossil energy.[1] As one half reaction of electrocatalytic water splitting, hydrogen evolution reaction (HER) has attracted increasing attention due to its massive potential in the industrial hydrogen production,[2] especially when the required electricity is generated from various renewable energy resources like wind, solar, water power and so on.[3] Although Pt is capable of excellent catalytic performance for the HER, the high cost and limited storage are constraints on its large-scale application. Mover, the commercial Pt/C operate well only at low current densities.[4] Therefore, it is highly desirable to develop a sort of electrocatalyst that is efficient, stable and cost effective for the HER.[5] Due to the similar d-band electronic structure to Pt and derived from the earth-abundant materials, Mo$_2$C has been considered as a promising candidate to substitute noble metal electrocatalysts for HER.[6] Despite this, there remain three issues that need to be addressed properly during the practical application of Mo$_2$C for HER. Firstly, it usually suffers from inevitable aggregation at high calcination temperatures during the synthesis process.[7] As a result of that, the density of active sites is reduced dramatically and the overpotential for HER is increased

sharply.[8] Secondly, in general, the Mo$_2$C shows poor conductivity. Furthermore, the negative hydrogen binding energy (ΔG_{H^*}) on Mo$_2$C indicates a strong adsorption of H on its surface, which imposes a significant restriction on the desorption process of H$_{ads}$ to generate H$_2$.[9] Thus, both will hinder its HER activity. Thirdly, due to the difference of HER mechanisms between in acidic and in alkaline conditions, it is common that Mo$_2$C shows slow water dissociation kinetics in an alkaline solution.[10] However, oxygen evolution reaction (OER) as the other half reaction of water splitting is usually operated in alkaline medium.[11] Therefore, if both HER and OER occurred in alkaline environment, it would make the device capable to operate in an easier and more economical way.[12] It is worth noting that the current densities widely used in alkaline electrolyzers for HER range from 200 to 500 mA cm^{-2} in practical industrial uses.[13] Thus, it is critical for Mo$_2$C to operate well at large current densities in alkaline solution.

In this study, these challenges were addressed through the design of 6~9 nm nitrogen-doped Mo$_2$C nanoparticles homogeneously decorated on 3D nitrogen-doped porous Mo$_2$C microflowers (0D/3D Mo$_2$C P/Mo$_2$C F) by applying a simple strategy. Notably, Mo–PMI$_m$ P were uniformly and firmly attached to the Mo–PMI$_n$ F, which ensured that no sintering occurred and a large number of active sites were exposed for Mo$_2$C P. The open framework of Mo$_2$C P/Mo$_2$C F not only endowed the sample with plenty of reaction sites, but also facilitated the penetration of electrolytes, transport of ions and release of hydrogen bubbles so as to exhibit a fast HER kinetics. The 0D/3D structure also increased its hydrophilia and was conducive to reducing the energy barrier of water dissociation and enhancing the HER activity in alkaline media. Furthermore, the introduction of nitrogen for Mo$_2$C improved H$^+$ adsorption and facilitated the process of H desorption from Mo–H, which was attributed to N atoms having better interaction with H$^+$

[a] Prof. Y. Sun,[+] Dr. F. Peng,[+] Prof. L. Zhang, Prof. B. Jiang, Dr. H. Dou, Dr. N. Zhang, Dr. M. Xu, Dr. N. Yang
School of Chemical Engineering and Technology
Tianjin University
Tianjin 300072 (P. R. China)
E-mail: yangnayna@tju.edu.cn

[+] These authors contributed equally to this work.

Supporting information for this article is available on the WWW under https://doi.org/10.1002/cctc.202000995

than C atoms and modifying the electronic structures of adjacent Mo and C atoms, respectively.[14] Benefitting from its nature of being Pt-like, nitrogen doping and 0D/3D specific structure, the prepared Mo_2C P/Mo_2C F exhibited large ECSA and j_0, low Tafel slope and small overpotential (at 1.0 and 10 mA cm^{-2}) in both alkaline and acidic electrolyte, suggesting its excellent HER activity and faster kinetics. Furthermore, it works better than commercial Pt/C at high current densities in 1.0 M KOH. As indicated by the desirable results, the synthesized Mo_2C P/Mo_2C F can be applied as a superior electrocatalyst for HER. Moreover, this study contributed a novel idea to the design of other nanoparticles such as Fe_xC, Co_xC, or V_xC dispersed on the 3D porous Mo_2C microflower through the calcination of their precursors consisting of co-precipitation of $Fe(CN)_6^{3-}$, $Co(CN)_6^{3-}$ or $NaVO_3$ with the cationic PMI_m dispersed on the surface of Mo–PMI_n F respectively, which can meet requirements of different applications.

2. Experimental section

2.1. Synthesis of PMI_n

The Poly (2, p-methylphenyl-ionene) (PMI_n) was synthesized by means of a simple Menshutkin reaction between TMEDA (Aladdin Reagent Co. Ltd., 99%) and 1,4-bis(chloromethyl) benzene (Alfa Aesar, 98%) (Figure S1), and the FT-IR spectra of PMI_n was shown in Figure S2.

2.2. Synthesis of Mo_2C F

Typically, 0.6 mmol PMI_n was dissolved into 46 mL deionized water prior to stirring for a period of 30 minutes. Then, 10 mL of 0.2 mmol ammonium molybdate (Aladdin Reagent Co. Ltd., 99%) solution was added into the PMI_n solution dropwise under magnetic stirring, which led to a white precipitate. After being thoroughly stirred at room temperature for a duration of 2 hours, the mixture was poured into a 100 mL Teflon-lined stainless-steel autoclave reactor and maintained at 100 °C for a spell of 10 hours. Then it was subjected to natural cool to room temperature and the solid Mo–PMI_n microflowers were collected by centrifugation, washed thoroughly with H_2O and ethanol and dried overnight inside a vacuum oven at 50 °C. Finally, Mo–PMI_n was annealed in a tube furnace at 700 °C at a slow temperature ramping rate of 2 °C min^{-1} for 120 minutes under an Ar (99.999%, Tianjin Dongxiang Specialty Gases Co., Ltd) atmosphere. Then, Mo_2C F was derived.

2.3. Synthesis of Mo_2C P/Mo_2C F

The preparation process of Mo–PMI_n nanoparticles decorated on Mo–PMI_n microflowers (Mo–PMI_m P/Mo–PMI_n F) was similar to that of Mo–PMI_n F, except that the solution after hydrothermal treatment was stirred for half an hour again at room temperature before being added dropwise with 5 mL of 0.03 mmol ammonium molybdate solution and stirred for 2 hours. Subsequently, the Mo–PMI_m P/Mo–PMI_n F was obtained by centrifugation, washed thoroughly with H_2O and ethanol, dried and subjected to pyrolysis under the identical conditions to and following the same procedures as the Mo–PMI_n microflowers. Then, the ultrafine nitrogen-doped Mo_2C nanoparticles decorated on 3D nitrogen-doped Mo_2C microflowers (Mo_2C P/Mo_2C F) were obtained.

2.4. Characterization

The FT-IR of the sample was record on a Bio-Rad FTS 6000 FT-IR spectrometer. The XRD analysis was conducted with the assistance of a Bruker diffractometer with Cu Kα radiation. The surface morphologies and structures of the samples were determined by using scanning electron microscopy (SEM) on FESEM S-4800 (Hitachi Corp, Japan), which was combined with energy dispersive spectrometer (EDS) to explore the distribution of elements in the catalysts. The nanostructure of the catalysts was further characterized with the assistance of transmission electron microscope (TEM) and high-resolution transmission electron microscope (HRTEM) performed with a JEM-2100 F (Rigaku Corp., Japan) field-emission transmission electron microscope (200 kV). X-ray photoelectron spectroscopy (XPS) was measured by using a spectrometer Escalab Xi+ equipped with monochromatic Al Kα radiation (150 W). Raman spectra was collected from a Renishaw inVia Plus Raman microscope with 532 nm laser excitation. The contact angles of water droplets (1.0 μL) on samples at environmental temperature were determined by using an optical contact angle & interface tension meter (SL200KS, KINO, USA). The specific surface area of the sample was measured with a micromeritics ASAP 2020. Thermogravimetric analysis (TGA, TA Instruments 2000) was carried out in Ar and air atmosphere with a ramping rate of 10 °C min^{-1} from 30 to 850 °C.

2.5. Electrochemical characterization

Electrochemical measurements were performed by applying a CHI 760E electrochemical workstation (Shanghai Chenhua Co., China) with a standard three-electrode system. A saturated calomel electrode (Hg/HgCl$_2$ in saturated KCl) and a mercury oxide electrode (Hg/HgO in 1 M KOH) were taken as the reference electrode in H_2SO_4 and KOH, respectively. A graphite rod was used as the counter electrode and a glass-carbon disk with a diameter of 3.0 mm loading the catalyst was employed as the working electrode. Experimentally, 5.0 mg of the catalyst was dispersed in a mixture of 700 μL of water, 250 μL of ethanol, and 50 μL of 5 wt% Nafion solution (Sigma-Aldrich Co. LLC.) and ultrasonicated for 45 minutes. Then, a homogeneous ink was obtained and 5.0 μL of the as-obtained ink was dropped on the glassy-carbon disk using a microliter syringe and then dried at room temperature. The calculated catalyst including the commercial Pt/C (Johnson Matthey Chemicals Limited, 20%) loadings were all 0.35 mg cm^{-2}. Electrochemical

ChemCatChem

Full Papers
doi.org/10.1002/cctc.202000995

**Chemistry
Europe**
European Chemical
Societies Publishing

measurements were performed in 0.5 M H_2SO_4 and 1.0 M KOH. Before the HER test, ten cycles of cyclic voltammetry (CV) were first conducted at 10 mV s^{-1} from 0 to -0.5 V (vs RHE) for the activation of the catalyst. The linear sweep voltammetry (LSV) curves were recorded at a scan rate of 5.0 mV s^{-1}. All potentials were referenced to a reversible hydrogen electrode (RHE). In 0.5 M H_2SO_4 (pH = 0.34), E (RHE) = E (SCE) + 0.242 + 0.059 × pH; in 1.0 M KOH (pH = 13.95), E (RHE) = E (Hg/HgO) + 0.098 + 0.059 × pH. In order to estimate the electrochemically active surface area (ECSA) of the samples, the double-layer capacitance (C_{dl}) was studied since it is proportional to ECSA, and the cyclic voltammetry (CV) tests were conducted within non-faradaic region at a variable scan rates from 20 to 100 mV s^{-1}.

3. Results and discussion

The ultrafine nitrogen-doped Mo_2C nanoparticles decorated on 3D nitrogen-doped Mo_2C microflowers (Mo_2C P/Mo_2C F) were prepared as schematically illustrated in Figure 1. Firstly, a 3D porous microflower (Mo–PMI_n F) was developed through the cooperative self-assembly of cationic polymer PMI_n and anionic $Mo_7O_{24}^{6-}$, with its morphology and size controlled by making adjustment to the temperature of hydrothermal reaction and the molar ratios of $Mo_7O_{24}^{6-}$ and PMI_n. If the initial amount of PMI_n was a little excessive, the residual PMI_n would be degraded to PMI_m and adsorbed on the Mo–PMI_n F to be PMI_m/Mo–PMI_n F following the hydrothermal reaction. Then $Mo_7O_{24}^{6-}$ was added again and then the co-precipitation (Mo–PMI_m P) of $Mo_7O_{24}^{6-}$ with cationic PMI_m occurred in situ on the surface of Mo–PMI_n F. Subsequently, the ultrafine Mo–PMI_m nanoparticles dispersed on 3D Mo–PMI_n flowers (Mo–PMI_m P/Mo–PMI_n F) were obtained. The Mo_2C P/Mo_2C F and Mo_2C F were prepared through annealing of Mo–PMI_n F and Mo–PMI_m P/Mo–PMI_n F under Ar atmosphere, respectively. It is worth noting that the cationic PMI_n served as both nitrogen and carbon sources. A further study was performed on the effect created by pyrolysis temperature on the performance of samples. Unless otherwise specified, Mo_2C P/Mo_2C F and Mo_2C F indicate that the hydrothermal temperature is 100 °C, the molar ratio of $Mo_7O_{24}^{6-}$ to PMI_n is 3.0:1 and the pyrolysis temperature is 700 °C for their precursors. If the Mo_2C F or Mo_2C P/Mo_2C F is followed by one suffix tag (Mo_2C F-x or Mo_2C P/Mo_2C F-x), × indicates that only the corresponding condition is changed while all other conditions remain unchanged. For example, Mo_2C F-750 suggests that the pyrolysis temperature is 750 °C while other preparation conditions are consistent with Mo_2C F. Similarly, Mo_2C P/Mo_2C F-90 indicates that only the hydrothermal temperature of its precursor is changed to 90 °C. Moreover, 1 mmol of ammonium molybdate and 5 mmol of PMI_n were ground and mixed evenly by mortar prior to annealed at 700 °C for a period of 2 hours under Ar atmosphere. Finally, the obtained sample was denoted as Mo_2C B.

The thermal decomposition of Mo–PMI_n under Ar was studied by thermogravimetric analysis. As shown in Figure S3, the weight loss between 650 and 800 °C is the consequence of molybdenum oxide reduced to molybdenum carbide and the decomposition of molybdenum carbide to metallic molybdenum. The crystalline phase composition of the catalysts was determined by means of X-ray diffraction (Figure 2a). The Mo_2C P/Mo_2C F (the pyrolysis temperature is 700 °C) clearly shows the characteristic diffraction peaks at 34.4°, 38.0°, 39.4°, 52.1°, 61.5°, 69.6°, 72.4°, 74.6°, and 75.5°, attributable to the (100), (002), (101), (102), (110), (103), (200), (112) and (201) planes of β–Mo_2C (JCPDS 35–0787).[15] When the pyrolysis temperature is raised to 750 °C, the characteristic diffraction peaks of β–Mo_2C are shown to be significantly sharper. However, the peak at 2θ = 40.5° of metallic molybdenum (JCPDS 42–1120) which was formed due
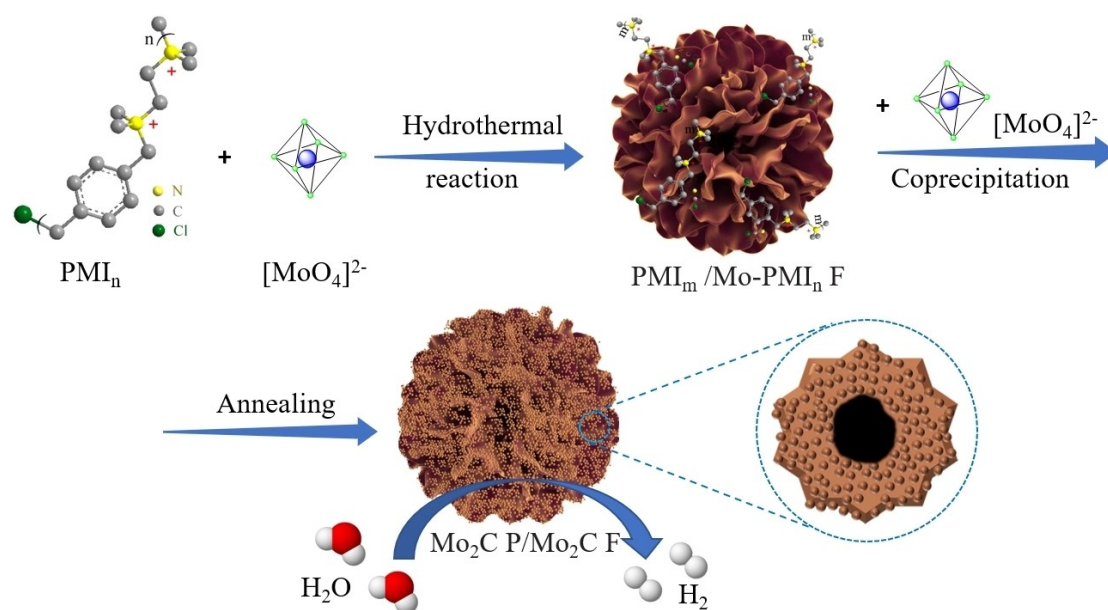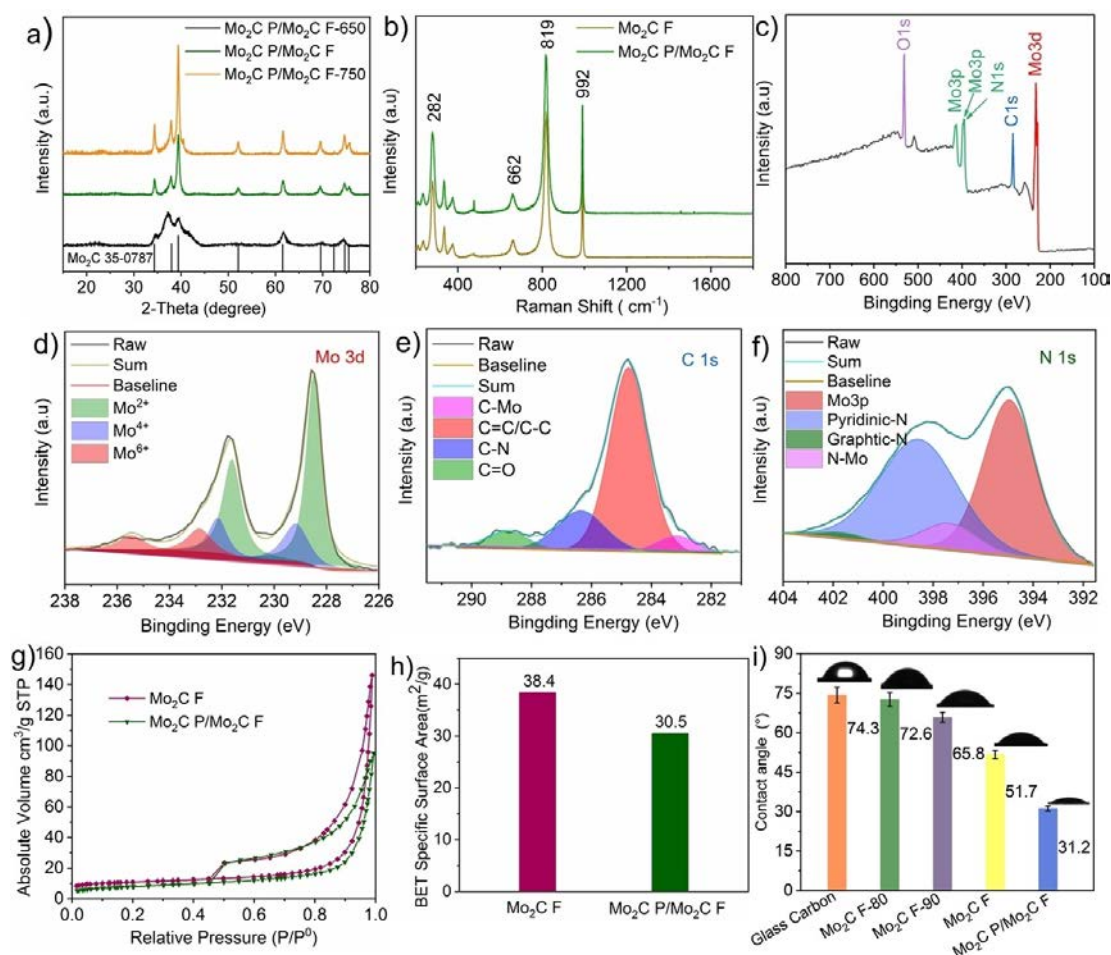

Figure 1. Schematic illustration of the synthesis process for Mo_2C P/Mo_2C F.

ChemCatChem

Full Papers
doi.org/10.1002/cctc.202000995

Chemistry
Europe
European Chemical
Societies Publishing

Figure 2. Physicochemical characterization. **a** XRD patterns of Mo_2C P/Mo_2C F-650, Mo_2C P/Mo_2C F, Mo_2C P/Mo_2C F-750. **b** Raman spectrum of Mo_2C F and Mo_2C P /Mo_2C F. **c** XPS survey spectra of the Mo_2C P/Mo_2C F sample; the corresponding high-resolution XPS spectra of (**d**) Mo 3d, (**e**) C 1s and (**f**) N 1s. **g** N_2 adsorption–desorption isotherm of Mo_2C F and Mo_2C P/Mo_2C F. **h** Corresponding BET specific surface area. **i** CAs of 1 μL water droplet on the surfaces of the catalysts after 30 seconds.

to the decomposition of some Mo_2C can be clearly observed. In addition, the characteristic diffraction peaks are less than obvious for Mo_2C P/Mo_2C F-650 when the calcination temperature is reduced to 650 °C, implying a poor crystallinity. Additionally, the XRD pattern of Mo_2C B is illustrated in Figure S4, suggesting that it is pure phase of β–Mo_2C. Therefore, only when the pyrolysis temperature reaches 700 °C, can the phase purity of Mo_2C P /Mo_2C F be at a high level. Moreover, the content of Mo_2C for the synthetic catalyst is affected by the pyrolysis temperature. From the thermal gravimetric analysis of Mo_2C P/Mo_2C F-650 and Mo_2C P/Mo_2C F-700, the content of Mo_2C is about 80.6% and 85.6% (Figure S5), respectively.

The catalysts were further characterized with Raman spectroscopy. Only Mo_2C peaks at 282, 662, 819, 992 cm^{-1} can be observed in the Raman spectrum (Figure 2b), demonstrating a pure phase of Mo_2C.[16] In order to gain insight into the electronic state and elemental composition of the surface of Mo_2C P/Mo_2C F, as a representative sample, X-ray photoelectron spectroscopy (XPS) was performed. As shown in Figure 2c, the surface is comprised of Mo, N, C, and O elements. The high-

resolution Mo 3d is fitted into three pairs of peaks (Figure 2d). The peaks located at 228.5 eV and 231.6 eV are assigned to the characteristic doublets Mo^{2+} ($3d_{5/2}$ and $3d_{3/2}$) of Mo_2C.[17] The other two pairs at 229.1 eV, 232.3 eV and 232.8 eV, 235.6 eV divulges the contribution from MoO_2 and MoO_3, respectively, produced by the unavoidable surface gradual oxidation of Mo_2C when exposed to air.[18] The spectrum of O 1s high-resolution XPS of Mo_2C P/Mo_2C F is illustrated in Figure S6. The peaks located at 530.9 eV are ascribed to oxygen ions ($O_{lattice}$) in molybdenum oxide.[19] The four XPS peaks of C 1s (Figure 2e) at 283.3, 284.7, 286.3 and 288.3 eV are associated with the C—Mo, C=C/C–C, C–N and C=O bond. As depicted in Figure 2f, the N 1s signal of the catalyst, derived from the N element in the Mo—PMI_m P/Mo—PMI_n F precursor, is capable to be deconvoluted into four different peaks. The peak located at 397.2 eV results from Mo–N bond, while the peaks centered at 398.6 eV and 401.9 eV can be ascribed to pyridinic N and graphitic N, respectively.[20] Moreover, the peak at binding energy of 394.8 eV results from Mo 3p peak overlapping with the N 1s peak.[21] The XPS peak of C–N, pyridinic N and graphitic N

ChemCatChem

Full Papers
doi.org/10.1002/cctc.202000995

Chemistry Europe
European Chemical
Societies Publishing

suggests a success of the N atoms being doped into the carbon matrix, and the peak of Mo−N bond proves that N atoms enter the Mo_2C lattice. In addition, it can be discovered that pyridine-N is the major type of doped N in Mo_2C P/Mo_2C F. The pyridine-N is able to increase the π state to the Fermi level with modifying the band density of carbon, and will be conducive to enhancing HER activity.[22]

An investigation was conducted into the specific surface areas (SSA) of the samples by means of N_2 adsorption. All of the nitrogen isothermal adsorption–desorption curves (Figure 2g, Figure S7a) are classed as type IV with a clear hysteresis loop resulting from the capillary condensation step, indicating that the catalysts possess a porous structure. As illustrated in (Figure 2h, Figure S7b), the SSA of Mo_2C F (38.4 $m^2 g^{-1}$) is larger than that of Mo_2C F-90 (29.5 $m^2 g^{-1}$) and Mo_2C F-80 (23.8 $m^2 g^{-1}$), which implies that the hydrothermal temperature of the precursor is a major influence factor for the catalysts. The SSA value of Mo_2C F-2.5 (23.6 $m^2 g^{-1}$) and Mo_2C F-3.5 (29.9 $m^2 g^{-1}$) are lower than that of Mo_2C F, indicating that the SSA of the sample is affected by the molar ratio of $Mo_7O_{24}^{6-}$ and PMI_n Moreover, the SSA of Mo_2C P/Mo_2C F and Mo_2C P/Mo_2C F-3.5 are smaller than that of Mo_2C F and Mo_2C F-3.5, respectively. This is attributed to the fact that the volume of pores on the 3D Mo_2C microflowers is reduced after being

decorated by Mo_2C nanoparticles, indicating a success of Mo_2C P being anchored on the 3D Mo_2C F.

In addition, a measurement was performed of the contact angles (CAs) for 1 μL of water droplet on their surfaces after the elapse of 30 seconds. The CAs are 74.3°, 72.6°, 65.8°, 51.7° and 31.2° for glass carbon electrode, Mo_2C F-80, Mo_2C F-90, Mo_2C F and Mo_2C P/Mo_2C F (Figure 2i), respectively. The contact angle of Mo_2C P/Mo_2C F is the minimum, indicating the most excellent wettability among all the samples under test. It is attributable to the increase in roughness of the surface after being decorated by nanoparticles. The excellent wettability of Mo_2C P/Mo_2C F will contribute to the access of the electrolyte and facilitate the release of hydrogen bubbles from its surface, thus promoting the efficiency of HER. Moreover, the strong affinity to water will be conducive to boost the alkaline Volmer step (* $+H_2O+e^-=$*H$+OH^-$) and the Heyrovsky step (H_2O+*H$+e^-=$*$+H_2+OH^-$), thus reducing the energy barrier of water dissociation and enhancing the HER activity in alkaline media.[6]

The specific microstructures of the samples were investigated by applying SEM and TEM. Figure 3a–h demonstrate that all the samples possess a 3D porous microflower structure, and that all of the microflowers are comprised of numerous radiating outward nanosheets with an average thickness of 10 nm. Not only does the open framework of 3D porous structure provide the samples with plenty of active sites, it also
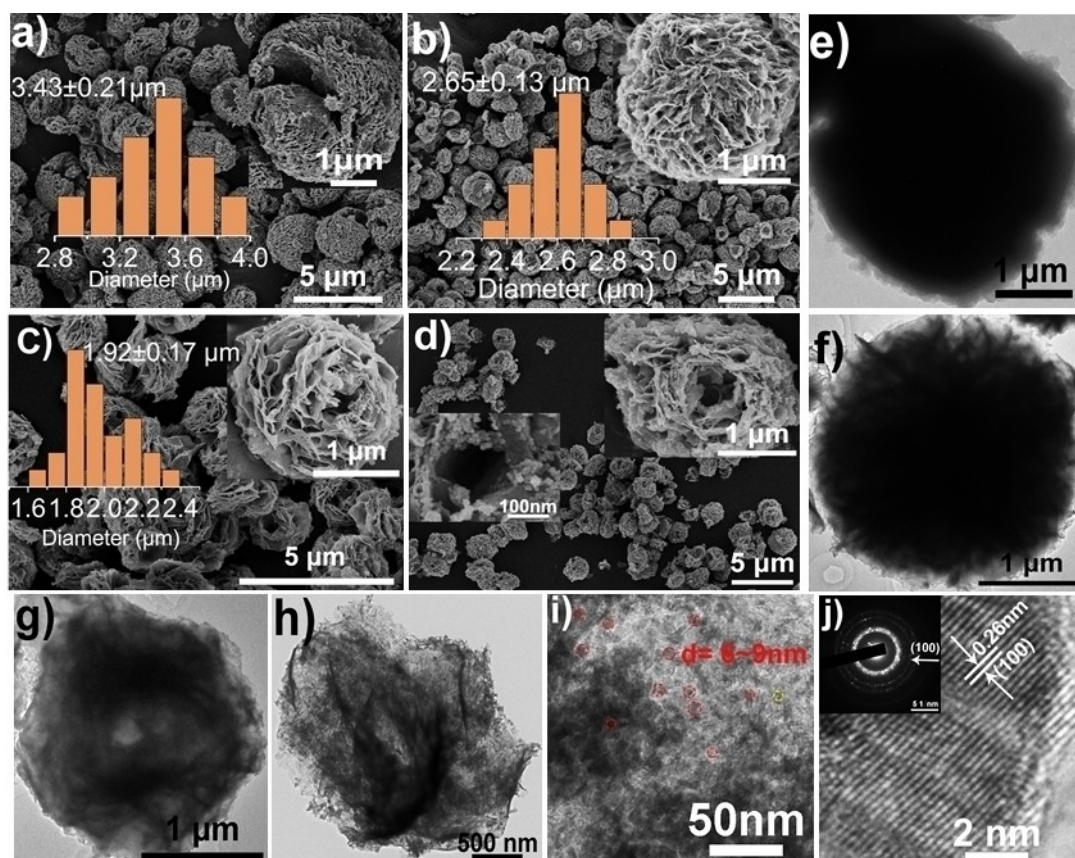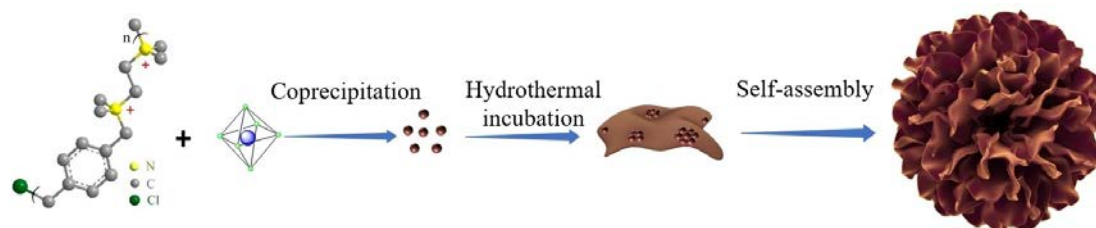

Figure 3. Morphology and structural characterization. **a–c** SEM images of Mo_2C F-80, Mo_2C F-90, Mo_2C F and their size distribution, respectively. The inset is an enlarged view of one microflower. **d** SEM image of Mo_2C P/Mo_2C F. Inset: its different enlarged views. **e–g** TEM images of Mo_2C F-80, Mo_2C F-90 and Mo_2C F, respectively. **h–i** TEM images of Mo_2C P/Mo_2C F. **j** HRTEM image of the region enclosed by the yellow circle of (**i**). Inset: the corresponding SEAD image.

expedites the diffusion of electrolyte and gas, which will be beneficial for better reaction kinetics and stability.[23] Interestingly, their specific morphology and diameter show difference. The interior of Mo$_2$C F (Figure 3c, g) and Mo$_2$C P/Mo$_2$C F (Figure 3d, h) are observed to be hollow and their diameter is shown to be ~1.9 μm. While the internal structures of Mo$_2$C F-80 (Figure 3a, e) and Mo$_2$C F-90 (Figure 3b, f) are found solid and their average sizes are shown to be ~2.7 μm and ~3.4 μm, respectively. Moreover, as revealed by Figures 3d and 3 h, the Mo$_2$C nanoparticles with a diameter ranging from 6 to 9 nm are scattered homogeneously and strongly in the Mo$_2$C microflower for Mo$_2$C P/Mo$_2$C F (Figure 3i). The Mo$_2$C F provides a three-dimensional (3D) scaffold for the distribution of 0D Mo$_2$C P, which is conducive to the development of 0D/3D Mo$_2$C P/Mo$_2$C F structure. The ultrasmall 0D Mo$_2$C nanoparticles will furnish a high density of HER active sites, for which the 0D/3D Mo$_2$C P/Mo$_2$C F will offer a much higher number of reaction sites than the bare 3D Mo$_2$C–F. Clear lattice fringe with a spacing of 0.26 nm can be observed from the HRTEM image, which corresponds to the (100) facet of β–Mo$_2$C. Besides, the selected-area electron diffraction (SAED) image exhibits the diffraction ring of (100) plane of β–Mo$_2$C (Figure 3j). Meanwhile, the morphology of Mo$_2$C F-2.0, Mo$_2$C F-2.5, Mo$_2$C F-3.5, Mo$_2$C P/Mo$_2$C F-3.5, Mo$_2$C P/Mo$_2$C F-90, Mo$_2$C F-110 and Mo$_2$C P/Mo$_2$C F-110 are also examined by conducting the SEM and TEM investigation (Figure 3a–i). The microflowers of Mo$_2$C F-2.0 and Mo$_2$C F-2.5 (Figure S8a, b) are incomplete and no nanoparticle is developed, implying that PMI$_n$ is insufficient for them. The diameter of Mo$_2$C F-3.5 is ~3.8 μm (Figure S8c), larger than 2.0 μm of Mo$_2$C F. In addition, the nanoparticles are severely agglomerated (Figure S8g) and the internal structure is solid (Figure S8i) for Mo$_2$C P/Mo$_2$C F-3.5. The diameter of Mo$_2$C F-110 is almost identical to that of Mo$_2$C F, except that the edges of the petals are partly curved and folded (Figure S8d), thus affecting the dispersion of Mo$_2$C nanoparticles for Mo$_2$C P/Mo$_2$C F-110 (Figure S8f). The above results demonstrate that both the hydrothermal temperature and the molar ratios of Mo$_7$O$_{24}^{6-}$ to PMI$_n$ of the precursor could make impact on the diameter, microstructure and the nanoparticles dispersion of the catalysts, which is facile to regulate the morphologies of samples for the practical needs of various applications. Therefore, they also affect the specific surface areas (SSA) and the tendency of their SSA conforms to that of their structures and diameters. Mo$_2$C P/Mo$_2$C F shows the minimum diameter and the most homogeneous distribution of nanoparticles among all the prepared

Mo$_2$C nanoparticles decorated on Mo$_2$C microflowers. Energy dispersive X-ray spectroscopic elemental mapping images (Figure S9) indicate the coexistence of Mo, C and N, which are distributed uniformly in Mo$_2$C P/Mo$_2$C F, suggesting successful N doping.

The morphologies of catalyst precursor over different hydrothermal incubation time was monitored by SEM (Figure S10a–d) to unveil the possible formation mechanism of 3D porous nanostructure. Upon the addition of Mo$_7$O$_{24}^{6-}$ into the PMI$_n$ solution, the Mo–PMI$_n$ was blocky and composed of small rough nanoparticles which was driven by the electrostatic interaction between the anion Mo$_7$O$_{24}^{6-}$ and the cationic PMI$_n$. After the hydrothermal incubation for 3 hours, the nanoparticles evolved into separate nanoflakes which were the petals of the microflowers as a result of the π–π stacking between benzene rings in PMI$_n$ and steric effect caused by rigid aromatic structure.[24] After 6 hours, the adjacent petals were adhered by PMI$_n$ which was functioned as a binder to form a porous nanostructure. After 10 hours, the petals on the surface were more tightly aligned and the anisotropic growth of petals contributed to the perfect 3D microflowers. The evolution process of Mo–PMI$_n$ is shown schematically illustrated in Figure 4 and proved by the results of SEM in Figure S10. In case the primary addition of PMI$_n$ was insufficient, the final morphology of Mo–PMI$_n$ microflowers was defective as a result of the deficient evolution processes of Mo–PMI$_n$ nanoparticles into Mo–PMI$_n$ nanoflakes or Mo–PMI$_n$ nanoflakes into Mo–PMI$_n$ microflowers. Therefore, the microflowers of Mo$_2$C F-2.0 (Figure S8a) and Mo$_2$C F-2.5 (Figure S8b) were incomplete. When the primary addition of PMI$_n$ was a large surplus, the diameter of Mo–PMI$_n$ microflower increased and the pore size decreased in that the petals thickened and cohered more tightly. Therefore, Mo$_2$C F-3.5 was bigger than Mo$_2$C F. In addition, when the hydrothermal temperature was low, the evolution rate of Mo–PMI$_n$ nanoparticles into Mo–PMI$_n$ nanoflakes decreased. As a result, some agglomerated Mo–PMI$_n$ nanoparticles acted as the core of the growth of the petals before they evolved into nanoflakes. Therefore, the interior of Mo$_2$C F-80 and Mo$_2$C F-90 was solid and the size was larger than Mo$_2$C F. Notably, as shown in Figure 3c and Figure S10d, the petals of microflower thinned and the pores broadened gradually during pyrolysis as a result of the decomposition of PMI$_n$.

In order to investigate the electrocatalytic HER (hydrogen evolution reaction) performance of the prepared samples, the linear sweep voltammetry (LSV) was first performed in 1 M KOH.

Figure 4. Schematic illustration of the evolution process of Mo–PMI$_n$.

ChemCatChem

Full Papers
doi.org/10.1002/cctc.202000995

Chemistry Europe
European Chemical
Societies Publishing

Meanwhile, the effect exerted by the annealing temperature on electrocatalytic HER property for Mo_2C P/Mo_2C F was investigated (Figure S11a, b), which led to the discovery that 700 °C calcination temperature is optimal. Mo_2C P/Mo_2C F-650 shows the lowest HER performance as a result of the low active sites caused by the poor crystallinity and lower content of Mo_2C. Mo_2C P/Mo_2C F-750 displays the lower HER activity as the metallic molybdenum has poor HER activity and may reduce the hydrophilicity of the catalyst. As shown in Figure 5a and Figure S12a Mo_2C P/Mo_2C F has the lowest overpotential value among all the prepared catalysts. It only requires an overpotential of 51 and 96 mV to deliver a current density of 1 and 10 mA cm^{-2}, respectively. In comparison, the overpotential for Mo_2C F to attain 1 mA cm^{-2} current density and 10 mA cm^{-2} current density (η_{10}) are 86 mV and 134 mV, respectively, which are found to be significantly larger than that of Mo_2C P/Mo_2C F. In this study, the overpotential at 1 mA cm^{-2} current density is defined as the onset overpotential (η_{onset}). Interestingly, the η_{onset} and η_{10} of Mo_2C P/Mo_2C F-110 (60 and 106 mV) and Mo_2C P/Mo_2C F-90 (68 and 116 mV) are notably lower than that of Mo_2C F-110 (90 and 139 mV) and Mo_2C F-90 (98 and 146 mV), respectively. As illustrated in Figure S12a, the η_{10} of Mo_2C P/

Mo_2C F-3.5 is 131 mV, exhibiting lower overpotential than that of Mo_2C F-3.5, Mo_2C F-2.5 and Mo_2C F-2.0. In comparison with the above results, it is obvious that all of the samples decorated by Mo_2C nanoparticles require smaller overpotential and show higher catalytic activity than the corresponding bare Mo_2C microflowers. It is widely known that, there are a large number of uncoordinated atoms and suspended bonds on the surface of nanoparticles, as a result of which 0D Mo_2C nanoparticles possess high density of active sites and excellent HER activity in theory. Nevertheless, nanoparticles are prone to aggregation during the process of calcination, and such irreversible aggregation will severely impede the catalytic activity of Mo_2C nanoparticles. In contrast, the 6~9 nm Mo_2C nanoparticles are scattered uniformly in the 3D Mo_2C microflower for 0D/3D Mo_2C P/Mo_2C F. This extraordinary structure combines the superiority of 0D nanoparticles and 3D porous microflower to bear plentiful active sites and facilitate the electrolyte and gas diffusion during the HER reaction. As a result of that, the 0D/3D Mo_2C P/Mo_2C F exhibits outstanding HER performance. Interestingly, the required overpotential is identical to attain 119 mA cm^{-2} for Mo_2C P/Mo_2C F and commercial Pt/C, and Mo_2C P/Mo_2C F works better than the commercial Pt/C at higher
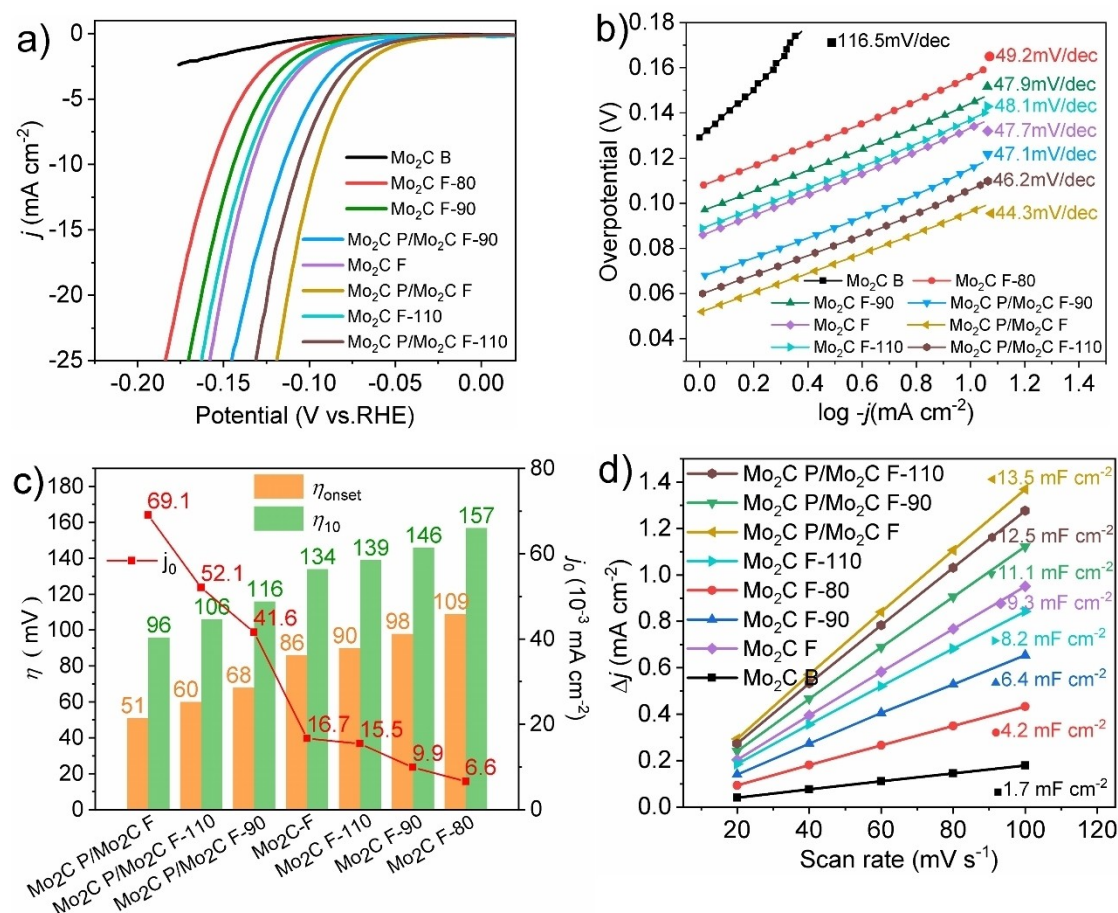
Figure 5. Electrochemical measurements in 1.0 M KOH. a HER polarization curves of Mo_2C B, Mo_2C F-80, Mo_2C F-90, Mo_2C F, Mo_2C F-110, Mo_2C P/Mo_2C F-90, Mo_2C P/Mo_2C F and Mo_2C P/Mo_2C F-110. b Corresponding Tafel slopes. c Corresponding η_{10}, onset overpotential values and j_0. d Electrochemical active surface area measurements.

ChemCatChem

Full Papers
doi.org/10.1002/cctc.202000995

Chemistry
Europe
European Chemical
Societies Publishing

current density in 1.0 M KOH (Figure S13). In comparison, Mo_2C B shows extremely poor HER activity with onset overpotential of 130 mV, significantly larger than that of 86 mV of Mo_2C F, suggesting that the 3D porous structure enables the catalysts to achieve efficient HER performance. Moreover, Mo_2C F manifests the highest HER activity among the Mo_2C microflowers without Mo_2C nanoparticles decorated on it, suggesting that the catalytic activity of Mo_2C can be easily adjusted by changing the hydrothermal temperature and molar ratios of $Mo_7O_{24}^{6-}$ to PMI_n for the precursor.

Subsequently, Tafel plots were analyzed to further validate the mechanism of HER. As presented in Figure 5b and Figure S12b, the Tafel slope of Mo_2C P/Mo_2C F is 44.3 mV/dec, lower than that of any other sample. This indicates an efficient dynamic process of hydrogen evolution. Interestingly, all the Tafel slopes of Mo_2C microflowers decorated by Mo_2C nanoparticles are invariably smaller than that of corresponding bare Mo_2C microflowers, which suggests that the reaction of H_2 evolution can be improved by nanoparticles scattered in the 3D Mo_2C microflower. It is obviously observed that the Tafel slopes of the catalysts range from 44.3 to 116.5 mV/dec, indicating that the reaction followed a Volmer-Heyrovsky mechanism that the H desorption from Mo−H restricts the rate of H_2 generation. Moreover, Mo_2C F exhibits a far inferior value of Tafel slope compared to that of Mo_2C B, confirming that the 3D porous

structure of Mo_2C F could accelerate the reaction of HER. Furthermore, the exchange current density (j_0) was obtained through extrapolating the linear fitted Tafel curves as described. As depicted in Figure 5c, Mo_2C P/Mo_2C F has the largest j_0 of 0.069 mA cm^{-2}, which is nearly four and ten folds larger than the j_0 of Mo_2C F (0.0167 mA cm^{-2}) and Mo_2C F-80 (0.006 mA cm^{-2}), respectively, demonstrating that the Mo_2C P/Mo_2C F features a larger number of electroactive sites and expedite HER kinetics. The ECSA of the samples were investigated as well by conducting the CV tests under alkaline conditions (Figure S14). The electrochemical double-layer capacitance (EDLC, C_{dl}) was calculated from the slope of the current density versus the sweep rate (Figure 5d). Particularly, the C_{dl} of Mo_2C P/Mo_2C F is 13.5 mF cm^{-2}, which is higher than those of other samples and almost eight times higher than that of Mo_2C B, which confirms that the 0D/3D structure of Mo_2C P/Mo_2C F has the capability to expose more abundant reaction sites for HER.

Apart from that, an assessment was made as well of the HER properties of some typical samples in 0.5 M H_2SO_4. The effect created by pyrolysis temperature on Mo_2C P/Mo_2C F was first investigated (Figure S11c, d), indicating that 700 °C pyrolysis temperature is also optimal for its HER activity in acidic solution. As shown in Figure 6a and c, as expected, Mo_2C P/Mo_2C F demonstrated the best activity. The η_{onset} and η_{10} of
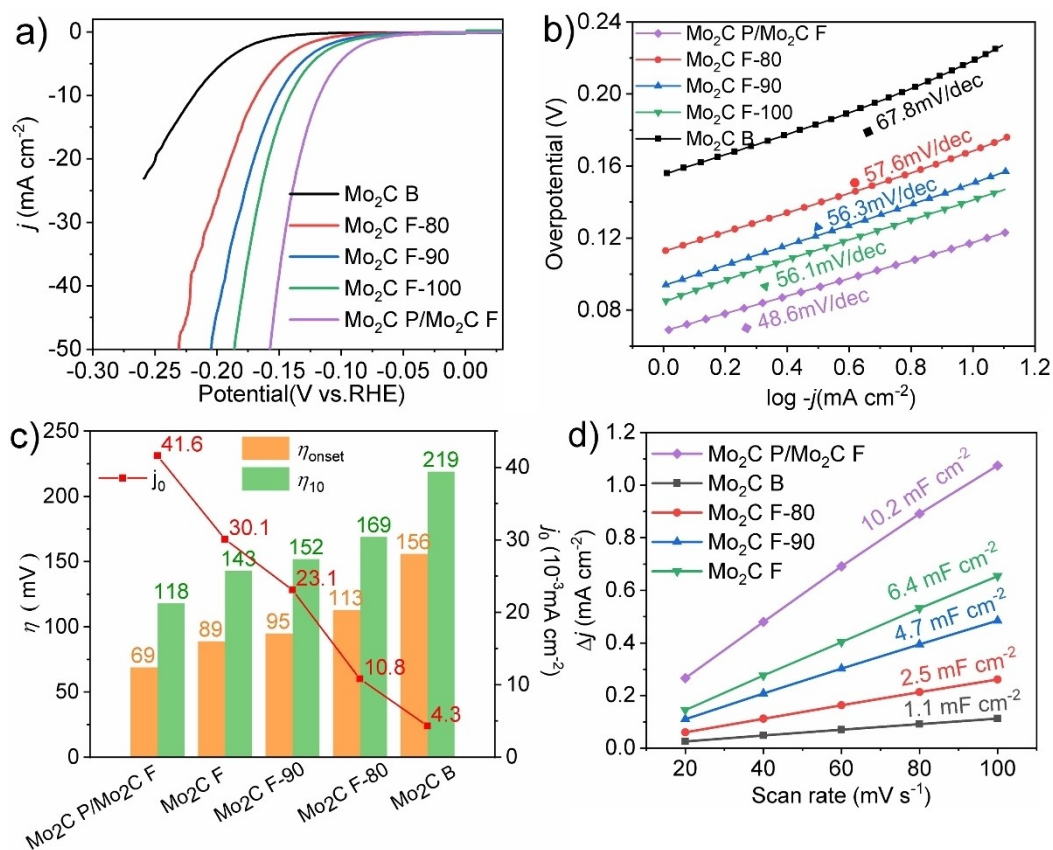
Figure 6. Electrochemical measurements in 0.5 M H_2SO_4. a HER polarization curves of Mo_2C B, Mo_2C F-80, Mo_2C F-90, Mo_2C F and Mo_2C P/Mo_2C F. b Corresponding Tafel slopes. c Corresponding η_{10}, onset overpotential values and j_0. d Electrochemical active surface area measurements.

ChemCatChem

Full Papers
doi.org/10.1002/cctc.202000995

Chemistry Europe
European Chemical
Societies Publishing

Mo$_2$C P/Mo$_2$C F are 69 mV and 118 mV, respectively, lower than those of Mo$_2$C F (89 mV, 143 mV), Mo$_2$C F-90 (95 mV, 152 mV) and Mo$_2$C F-90 (113 mV, 169 mV). In addition, Mo$_2$C B requires an overpotential of 156 mV and 219 mV to reach a current density of 1 and 10 mA cm^{-2}, respectively, indicating the relatively poor performance, and evidencing the superiority of the 3D porous microflower. Consistent with the LSV curves, the Tafel slope of Mo$_2$C P/Mo$_2$C F is 48.6 mV/dec, smaller than that of Mo$_2$C F (56.1 mV/dec), Mo$_2$C F-90 (56.3 mV/dec), Mo$_2$C F-80 (57.6 mV/dec) and Mo$_2$C B (67.8 mV/dec) (Figure 6b). As shown in Figure S12c and d, the η_{10} and Tafel slope of Mo$_2$C F 2.0–3.5 and Mo$_2$C P/Mo$_2$C F-3.5 are significantly larger than those of Mo$_2$C F and Mo$_2$C P/Mo$_2$C F, respectively. Based on the above results of Tafel slope, it can be concluded that the reaction also followed a Volmer-Heyrovsky mechanism in acid solution. Notably, Mo$_2$C P/Mo$_2$C F shows the highest j_0 of 0.042 mA cm^{-2}, almost ten times larger than that of Mo$_2$C B. Furthermore, the ECSA was also investigated by conducting the cyclic voltammetry (CV) tests (Figure S15) in acidic environment. The C$_{dl}$ of Mo$_2$C P/Mo$_2$C F is 10.2 mF cm^{-2}, substantially larger than that of other samples (Figure 6d).

The electrocatalytic stability is another important criterion for a practical catalyst. The LSV curves of Mo$_2$C P/Mo$_2$C F are presented in Figure 7a, where only a slight shift can be observed after 10,000 cycles, and the inset of Figure 7a shows that nearly no current decrease could be observed after 18 hours. Additionally, the current time profile of chronoamperometry (Figure S16) at an overpotential of 0.17 V (vs RHE) for 10 hours in 1 M KOH shows that Mo$_2$C P/Mo$_2$C F was more stable than the commercial Pt/C. both indicating its superior HER stability. Meanwhile, the microstructures of the Mo$_2$C P/Mo$_2$C F after the test of durability were also examined. As shown in Figure S17a and b, despite the Mo$_2$C P/Mo$_2$C F was covered by the membrane of Nafion, we could also clearly observe that the 3D porous structure was well maintained and the nanoparticles were still anchored tightly on the surface of Mo$_2$C F. It is also worth noting that the HER performance of Mo$_2$C P/Mo$_2$C F outperforms many other Mo$_2$C-based catalysts ever reported (Figure 7b, c),[25] suggesting more excellent HER activity and faster kinetics.

In addition, Fe$_x$C P/Mo$_2$C F, Co$_x$C P/Mo$_2$C F and V$_x$C P/Mo$_2$C F were also synthesized through the calcination of their precursors consisting of co-precipitation of Fe(CN)$_6^{3-}$, Co(CN)$_6^{3-}$ and NaVO$_3$ with the cationic PMI$_m$ dispersed on the surface of Mo–PMI$_n$ F, respectively. The specific microstructure, elemental composition and distribution of the samples were investigated by applying SEM, XPS, EDS and TEM (Figure S18–21), respectively. The SEM and TEM pictures of the samples display that Fe$_x$C, Co$_x$C and V$_x$C were all nanoparticles scattered in the Mo$_2$C F. The EDS images indicate that Fe, Co and V are distributed uniformly on the surface of the samples, respectively. The XPS pictures show the existence and electronic state of Fe, Co and V, respectively.

4. Conclusions

In this study, a novel ultrasmall nitrogen-doped Mo$_2$C nanoparticles homogeneously decorated on 3D nitrogen-doped porous Mo$_2$C microflowers was designed and synthesized. The morphology and diameter of 3D porous Mo$_2$C can be tuned in an easy and precise way. A combination of large ECSA and j_0, low Tafel slope and small η_{onset} and η_{10} of Mo$_2$C P/Mo$_2$C F in both alkaline and acidic media, and better performance than commercial Pt/C at high current densities in alkaline solution demonstrates its excellent HER performance. It can reasonably be attributed to its nature of being Pt-like, nitrogen doping, 0D/3D specific structure. The 0D/3D structure of Mo$_2$C P/Mo$_2$C F exposed plentiful active sites as well as enhanced electrolyte and gas diffusion. Its excellent wettability facilitated water dissociation in alkaline media. As revealed by the excellent results, the 0D/3D Mo$_2$C P/Mo$_2$C F can be applied as an ideal catalyst for HER. Moreover, this study provided a novel strategy for the design of other M$_x$C (M=Fe, Co or V) nanoparticles dispersed on the 3D porous Mo$_2$C microflowers forming M$_x$C P/Mo$_2$C F to meet the requirements of different applications.
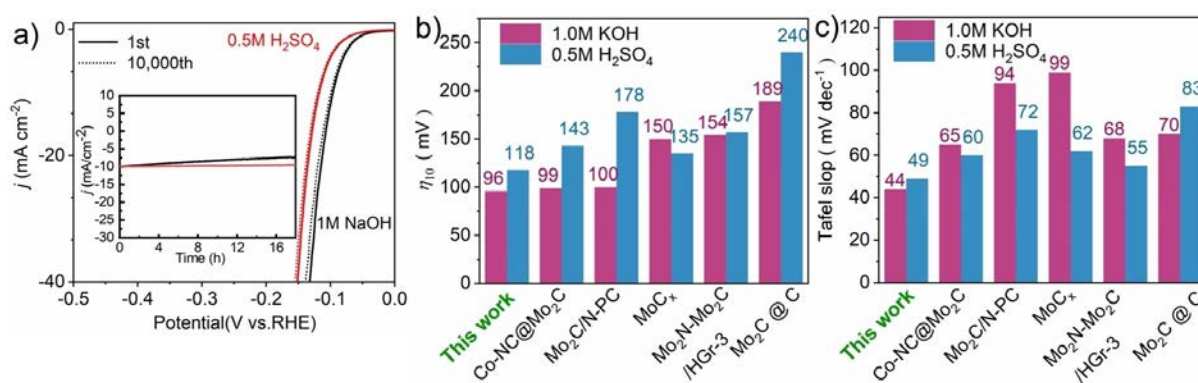
Figure 7. a Polarization curves of Mo$_2$C P/Mo$_2$C F before and after 10000 cycles. b–c Comparison of η_{10} and Tafel slops of this work with the reported Mo$_2$C-based catalysts, respectively.

ChemCatChem

Full Papers
doi.org/10.1002/cctc.202000995

Chemistry Europe
European Chemical
Societies Publishing

[1] a) G. Yang, B. Zhang, J. Wang, M. Wang, S. Xie, X. Li, *J. Sol-Gel Sci. Technol.* **2016**, *77*, 335–341; b) X. Zhang, J. Wang, T. Guo, T. Liu, Z. Wu, L. Cavallo, Z. Cao, D. Wang, *Appl. Catal. B* **2019**, *247*, 78–85.

[2] a) P. Wang, J. Qi, X. Z. Chen, C. A. Li, T. H. Wang, C. H. Liang, *Int. J. Hydrogen Energy* **2017**, *42*, 10880–10890; b) W. C. Xu, S. L. Zhu, Y. Q. Liang, Z. D. Cui, X. J. Yang, A. Inoue, *J. Mater. Chem. A.* **2018**, *6*, 5574–5579.

[3] a) Y. T. Luo, L. Tang, U. Khan, Q. M. Yu, H. M. Cheng, X. L. Zou, B. L. Liu, *Nat. Commun.* **2019**, *10*, 269; b) Y. Pan, K. A. Sun, S. J. Liu, X. Cao, K. L. Wu, W. C. Cheong, Z. Chen, Y. Wang, Y. Li, Y. Q. Liu, D. S. Wang, Q. Peng, C. Chen, Y. D. Li, *J. Am. Chem. Soc.* **2018**, *140*, 2610–2618; c) L. R. L. Ting, Y. L. Deng, L. Ma, Y. J. Zhang, A. A. Peterson, B. S. Yeo, *ACS Catal.* **2016**, *6*, 861–867.

[4] a) Y. Q. Deng, Z. Liu, A. Z. Wang, D. H. Sun, Y. K. Chen, L. J. Yang, J. B. Pang, H. Li, H. D. Li, H. Liu, W. J. Zhou, *Nano Energy* **2019**, *62*, 338–347; b) L. J. Yang, Y. Q. Deng, X. F. Zhang, H. Liu, W. J. Zhou, *Nanoscale* **2018**, *10*, 9268–9275.

[5] a) Z. W. She, J. Kibsgaard, C. F. Dickens, I. Chorkendorff, J. K. Nørskov, T. F. Jaramillo, *Science* **2017**, *355*; b) M. Zeng, Y. Li, *J. Mater. Chem. A.* **2015**, *3*, 14942–14962; c) X. X. Zou, Y. Zhang, *Chem. Soc. Rev.* **2015**, *44*, 5148–5180; d) S. Y. Jing, J. J. Lu, G. T. Yu, S. B. Yin, L. Luo, Z. D. Zhang, Y. G. Ma, W. Chen, P. K. Shen, *Adv. Mater.* **2018**, *28*, 1705979.

[6] a) G. Li, D. Zhang, Y. Yu, S. Huang, W. Yang, L. Cao, *J. Am. Chem. Soc.* **2017**, *139*, 16194–16200; b) J. Staszak-Jirkovský, C. D. Malliakas, P. P. Lopes, N. Danilovic, S. S. Kota, K. C. Chang, B. Genorio, D. Strmcnik, V. R. Stamenkovic, M. G. Kanatzidis, N. M. Markovic, *Nat. Mater.* **2016**, *15*, 197–203; c) Z. Kou, T. Wang, Y. Cai, C. Guan, Z. Pu, C. Zhu, Y. Hu, A. M. Elshahawy, J. Wang, S. Mu, *Small Methods* **2018**, *4*, 1700396; d) M. Miao, J. Pan, T. He, Y. Yan, B. Y. Xia, X. Wang, *Chem. Eur. J.* **2017**, *23*, 10947–10961.

[7] a) Y. Huang, X. N. Song, J. Deng, C. Y. Zha, W. J. Huang, Y. L. Wu, Y. G. Li, *Appl. Catal. B* **2019**, *245*, 656–661; b) J. X. Feng, J. Q. Wu, Y. X. Tong, G. R. Li, *J. Am. Chem. Soc.* **2018**, *140*, 610–617.

[8] a) Q. Gao, W. Zhang, Z. Shi, L. Yang, Y. Tang, *Adv. Mater.* **2019**, *31*, e1802880; b) D. Hou, S. Zhu, H. Tian, H. Wei, X. Feng, Y. Mai, *ACS Appl. Mater. Interfaces* **2018**, *10*, 40800–40807.

[9] a) R. Michalsky, Y. J. Zhang, A. A. Peterson, *ACS Catal.* **2014**, *4*, 1274–1278; b) J. S. Sun, Z. Wen, L. P. Han, Z. W. Chen, X. Y. Lang, Q. Jiang, *Adv. Funct. Mater.* **2018**, *28*, 1706127.

[10] a) B. Gao, X. Du, Y. Ma, Y. Li, Y. Li, S. Ding, Z. Song, C. Xiao, *Appl. Catal. B* **2019**, *263*, 117750; b) S. Y. Jing, L. S. Zhang, L. Luo, J. J. Lu, S. B. Yin, P. K. Shen, P. Tsiakaras, *Appl. Catal. B* **2018**, *224*, 533–540; c) L. F. Shen, B. A. Lu, X. M. Qu, J. Y. Ye, J. M. Zhang, S. H. Yin, Q. H. Wu, R. X. Wang, S. Y. Shen, T. Sheng, Y. X. Jiang, S. G. Sun, *Nano Energy* **2019**, *62*, 601–609.

[11] a) L. Zeng, K. Sun, X. Wang, Y. Liu, Y. Pan, Z. Liu, D. Cao, Y. Song, S. Liu, C. Liu, *Nano Energy* **2018**, *51*, 26–36; b) M. Yu, Z. Wang, J. Liu, F. Sun, P. Yang, J. Qiu, *Nano Energy* **2019**, *63*, 103880; c) M. J. Kenney, J. E. Huang, Y. Zhu, Y. T. Meng, M. Q. Xu, G. Z. Zhu, W. H. Hung, Y. Kuang, M. C. Lin, X. M. Sun, W. Zhou, H. J. Dai, *Nano Res.* **2019**, *12*, 1431–1435.

[12] a) C. Lu, D. Tranca, J. Zhang, F. N. Rodri Guez Hernandez, Y. Su, X. Zhuang, F. Zhang, G. Seifert, X. Feng, *ACS Nano* **2017**, *11*, 3933–3942; b) C. Guan, C. Xiao, H. Wu, X. Liu, W. Zang, H. Zhang, J. Ding, Y. P. Feng, S. J. Pennycook, J. Wang, *Nano Energy* **2018**, *48*, 73–80.

[13] a) W. Gao, Y. Shi, Y. Zhang, L. Zuo, H. Lu, Y. Huang, W. Fan, T. Liu, *ACS Sustainable Chem. Eng.* **2016**, *4*, 6313–6321; b) H. F. Wei, Q. Y. Xi, X. Chen, D. Y. Guo, F. Ding, Z. Yang, S. Wang, J. Li, S. M. Huang, *Adv. Sci.* **2018**, *3*, 1700733.

[14] H. Lin, N. Liu, Z. Shi, Y. Guo, Y. Tang, Q. Gao, *Adv. Funct. Mater.* **2016**, *26*, 5590–5598.

[15] Z. K. Kou, L. Zhang, Y. Y. Ma, X. M. Liu, W. J. Zang, J. Zhang, S. Z. Huang, Y. H. Du, A. K. Cheetham, J. Wang, *Appl. Catal. B* **2019**, *243*, 678–685.

[16] L. F. Pan, Y. H. Li, S. Yang, P. F. Liu, M. Q. Yu, H. G. Yang, *Chem. Commun.* **2014**, *50*, 13135–13137.

[17] a) L. Ji, J. Wang, L. Guo, Z. Chen, *J. Mater. Chem. A.* **2017**, *5*, 5178–5186; b) J.-Q. Chi, J.-W.-K. Gao, J.-H. Lin, B. Dong, J.-F. Qin, Z.-Z. Liu, B. Liu, Y.-M. Chai, C.-G. Liu, *J. Catal.* **2018**, *360*, 9–19.

[18] a) J. Halim, S. Kota, M. R. Lukatskaya, M. Naguib, M. Q. Zhao, E. J. Moon, J. Pitock, J. Nanda, S. J. May, Y. Gogotsi, M. W. Barsoum, *Adv. Funct. Mater.* **2016**, *26*, 3118–3127; b) J. J. Wang, W. Wang, Z. Y. Wang, J. G. G. Chen, C. J. Liu, *ACS Catal.* **2016**, *6*, 6585–6590.

[19] P. Thangasamy, N. Ilayaraja, D. Jeyakumar, M. Sathish, *Chem. Commun. (Camb.)* **2017**, *53*, 2245–2248.

[20] J. Wang, J. Chen, T. Wang, N. Bate, C. Wang, E. Wang, *Nano Res.* **2018**, *11*, 4535–4548.

[21] a) C. B. Lu, D. Tranca, J. Zhang, F. R. Hernandez, Y. Z. Su, X. D. Zhuang, F. Zhang, G. Seifert, X. L. Feng, *ACS Nano* **2017**, *11*, 3933–3942; b) Z. L. Wang, H. Luo, R. Lin, H. Lei, Y. F. Yuan, Z. L. Zhu, X. B. Li, W. J. Mai, *Appl. Catal. B* **2019**, *257*, 117891.

[22] a) H. Tabassum, W. Guo, W. Meng, A. Mahmood, R. Zhao, Q. Wang, R. Zou, *Adv. Energy Mater.* **2017**, *9*, 1601671; b) X. Gao, H. Zhang, Q. Li, X. Yu, Z. Hong, X. Zhang, C. Liang, Z. Lin, *Angew. Chem. Int. Ed.* **2016**, *55*, 6290–6294; *Angew. Chem.* **2016**, *128*, 6398–6402.

[23] a) J. Q. Chi, W. K. Gao, J. H. Lin, B. Dong, J. F. Qin, Z. Z. Liu, *J. Catal.* **2018**, *360*, 9–19; b) J. H. Yan, Y. Xie, Y. Jiao, A. Wu, C. Tian, X. Zhang, *Adv. Mater.* **2018**, *30*, 1704156.

[24] C. X. Xia, Z. Wang, D. Sun, B. L. Jiang, X. Xin, *Langmuir* **2017**, *33*, 13242–13251.

[25] H. B. Wu, B. Y. Xia, L. Yu, X. Y. Yu, X. W. Lou, *Nat. Commun.* **2015**, *6*, 6512.